Suzaku observations of Jovian diffuse hard X-ray emission

Masaki Numazawa[1,*], **Yuichiro Ezoe**[1], **Takaya Ohashi**[1], **Kumi Ishikawa**[2], **Yoshizumi Miyoshi**[3], **Daikou Shiota**[3,4], **Yasunobu Uchiyama**[5], **Tomoki Kimura**[6] and **Graziella Branduardi-Raymont**[7]

[1]Department of Physics, Tokyo Metropolitan University, 1-1 Minami-Osawa, Hachioji, Tokyo 192-0397, Japan

[2]The Institute of Space and Astronautical Science (ISAS), Japan Aerospace and Exploration Agency (JAXA), 3-1-1 Yoshinodai, Chuo-ku, Sagamihara 229-8510, Japan

[3]Institute for Space-Earth Environmental Research, Nagoya University, Furo-cho, Chikusa-ku, Nagoya 464-8601, Japan

[4]Applied Electromagnetic Research Institute, National Institute of Information and Communications Technology, 4-2-1 Nukui-Kita, Koganei, Tokyo 184-8795, Japan

[5]Department of Physics, Rikkyo University, 3-34-1 Nishi-Ikebukuro, Toshima-ku, Tokyo 171-8501, Japan

[6]Department of Geophysics, Tohoku University, 6-3 Aramaki, Aoba-ku, Sendai 980-8578, Japan

[7]Mullard Space Science Laboratory, University College London, Holmbury St Mary, Dorking RH5 6NT, Surrey, United Kingdom

*E-mail: masaki.numazawa@riken.jp, numazawa.masaki.phd2020@gmail.com

Abstract

We report on results of systematic analyses of the entire three X-ray data sets of Jupiter taken by Suzaku in 2006, 2012, and 2014. Jovian diffuse hard X-ray emission was discovered by Suzaku in 2006 when the solar activity went toward its minimum. The diffuse emission was spatially consistent with the Jovian inner magnetosphere and was spectrally fitted with a flat power-law function suggesting non-thermal emission. Thus, a scenario in which ultra-

relativistic (tens MeV) electrons in the Jovian inner magnetosphere inverse-Comptonize solar visible photons into X-ray bands has been hypothetically proposed. We focused on the dependence of the Jovian diffuse hard X-ray emission on the solar activity to verify this scenario. The solar activity in 2012 and 2014 was around the maximum of the 24th solar cycle. By combining the imaging and spectral analyses for the three data sets, we successfully separated the contribution of the diffuse emission from the emission of Jupiter's body (i.e., the aurora and disk emission). The 1–5 keV luminosity of the diffuse emission has been stable and did not vary significantly, and did not simply depend on the solar activity, which is also known to scarcely affect the high-energy electron distribution in the Jovian inner magnetosphere. The luminosity of the body emission both in 0.2–1 and 1–5 keV, in contrast, probably depended on the solar activity and varied by a factor of 2–5. These results strongly supported the inverse-Compton scattering scenario by the ultra-relativistic electrons. In this paper, we estimate spatial and spectral distributions of the inverse-Compton scattering X-rays by Jovian magnetospheric high-energy electrons with reference to the Divine&Garrett model and found a possible agreement in an inner region ($\lesssim$10 R_J) for the X-ray observations.

Key words: planets and satellites: general — planets and satellites: individual(Jupiter) — X-rays: general

---

1 Introduction

As one of the forefront of space observations, X-rays from solar system objects have been detected (Bhardwaj et al. 2007). The discovery of planetary X-rays was made in the 1950s from the Earth's aurora. Later, the Einstein satellite detected X-ray emission from Jupiter in 1979 (Metzger et al. 1983), and those from the heliosphere and the Earth's upper atmosphere in the 1990s. Resent observatories such as Chandra, XMM-Newton, and Suzaku brought dramatic progress in the investigation of the planetary X-ray emission. Chandra not only provided high-resolution X-ray images of the Earth and Jupiter but also discovered X-ray emission from Venus, Mars, and Saturn. XMM-Newton and Suzaku contributed much to the elucidation of mechanisms of the X-ray emission from such planets with their spectral capabilities.

Jupiter, the largest planet in our solar system, has an overwhelmingly huge and powerful

magnetosphere whose size is variable in a range of 50–100 R_J (Jupiter radii; 1 R_J = 7.1492 $\times 10^4$ km) in the solar direction and extends nearly to $\sim$10000 R_J in the opposite direction (see, e.g., Bagenal et al. 2004). Past satellite explorations and ground-based observations have discovered unique features of the Jovian magnetosphere such as aurorae, radiation belts, and Io plasma torus. They have especially found the existence of ultra-relativistic electrons with several tens of MeV in the Jovian magnetosphere. Since the discovery, we have a remaining issue how Jupiter accelerates such high-energy particles in its system inside.

X-ray observations of Jupiter can possibly solve the issue. Jupiter is also the most luminous X-ray source in the solar system excluding the Sun (Metzger et al. 1983; Waite et al. 1997). The recent observatories have been successfully and gradually revealing the emission mechanism of X-rays from Jupiter. In our general knowledge, the X-rays from Jupiter mainly consist of three emitting regions: aurora, disk, and its surrounding within a few tens R_J. We explain the mechanism of each part in the following text.

Chandra carried out the observations of Jupiter's X-ray aurora and showed a clear spectral signature of oxygen line emission and the location to be a high-latitude region that could be mapped to near the magnetopause boundary (Gladstone et al. 2002; Elsner et al. 2005). If the X-ray aurora was observed at low latitudes, this region could be connected to the middle magnetosphere (10–40 R_J) where there was sufficient phase space density of energetic sulfur and oxygen ions to account for the X-ray emission. However, the high aurora latitudes were connected to the outer magnetosphere ($>$40 R_J) which lacked the density of energetic heavy ions to provide the measured X-ray intensity. This result recalled the possibility of the existence of acceleration of energetic ions to increase the phase space distribution and the question of whether the acceleration involved magnetospheric heavy ions or solar wind heavy ions (Horanyi et al. 1988), which may now be answered: both of them are likely to contribute equally (Bunce et al. 2004; Kharchenko et al. 2008).

Subsequent spectral observations of Jupiter's auroral emission were conducted from XMM-Newton whose X-ray detector had medium and high energy resolution (Branduardi-Raymont et al. 2007a; Branduardi-Raymont et al. 2008; Branduardi-Raymont et al. 2004). The observations showed very strong emission lines of He-like oxygen. Charge exchange (CX) reaction caused by heavy ions from Io plasma source or solar winds produces these X-ray lines observed by Chandra and XMM-Newton. Besides, XMM-Newton, for the first time, identified a higher energy continuum component in the auroral spectra which was variable on a time scale of days. Researches based on simulations, the past X-ray observations from the Earth orbit, and *in-situ* measurements (especially by Juno) provided a plausible view in which the auroral

3

high-energy emission was caused by ion precipitation into the Jupiter's polar-caps (Cravens et al. 1995; Houston et al. 2020). The variability of the continuum spectrum was caused by a change of energy distribution of such particles in the Jovian magnetosphere or by an increase of the solar activity during the observation period, November 2003 (Branduardi-Raymont et al. 2007a).

Chandra displayed not only the auroral hot spot but also a relatively uniform distribution of X-rays covering the entire Jupiter's disk at low latitude (Gladstone et al. 2002). XMM-Newton also clearly showed a difference in spectral shape between the disk and auroral emission (Branduardi-Raymont et al. 2007b). The disk X-ray spectrum peaked at higher energy than the aurora, lacked the high energy bremsstrahlung, which was present in the latter, and was well fitted by a coronal plasma model with a temperature in the range 0.4–0.5 keV and solar abundance, by including additional MgXI and SiXIII emission lines at 1.35 and 1.86 keV, respectively. These lines in the spectra were likely to be caused by the solar activity, i.e., the solar abundance, which was enhanced at the time of observation. The conclusions obtained from the spectral studies of Jupiter were strengthened by the observation, again in November 2003 by XMM-Newton, of similar day-to-day variability in the solar and Jovian equatorial X-ray fluxes. A large solar X-ray flare, which occurred on the Jupiter-facing side of the Sun, was accompanied by a corresponding feature in Jupiter's disk X-ray lightcurve (see figure 30 in Branduardi-Raymont et al. 2007b). This finding supported the view reported by Maurellis et al. (2000) that indeed Jupiter's low latitude X-rays were mostly scattered radiation of solar origin.

Suzaku deeply observed Jupiter in February 2006 and discovered extended X-ray emission in 1–5 keV around Jupiter (Ezoe et al. 2010), with its comparative advantage in the sensitivity for such extended emission. The spatial distribution of the extended emission was roughly approximated by an ellipse-like shape with a size of $12\,\mathrm{R_J} \times 4\,\mathrm{R_J}$. This indicates an association with Jupiter's inner radiation belt (inner magnetosphere; $<10\,\mathrm{R_J}$) where high-energy electrons from keV reaching up to several tens of MeV exist. The spectral feature well-fitted by a flat power-law with a photon index $\sim$1.4 strongly suggested non-thermal emission. The luminosity estimated from the power-law spectral fit in 1–5 keV was 3.3×10^{15} erg s^{-1}, which was as large as that of the auroral emission within a factor of 2–3. Ezoe et al. (2010) discussed a possibility that the emission is likely to be produced via an inverse-Compton scattering of solar visible photons by Jovian magnetospheric electrons with extremely high energies (tens of MeV).

If the diffuse emission originates from such ultra-relativistic electrons, its variation am-

plitude should be similar to that of Jovian synchrotron radio (JSR) emission at a level of several tens of %. The JSR emission is considered to be produced by electrons with such high energies within several R_J from Jupiter, where the magnetic field is significantly strong (Bagenal et al. 2004; Bolton et al. 2002; Santos-Costa et al. 2008). The JSR emission shows both short (Miyoshi et al. 1999; Santos-Costa et al. 2008) and long-term variations as shown in figure 3 in Bolton et al. (2002), but does not indicate a simple correlation with the solar activity. The diffuse emission was again detected from an additional Suzaku observation in 2014 (Numazawa et al. 2019). They found that the luminosity of the diffuse emission showed relatively less variation than that of the aurora and disk. This result indicated that the diffuse emission is not simply depending on the solar activity as the JSR.

Since the environment is occupied by plasmas with energetic particles, it is difficult for exploration satellites to directly enter the region and only limited information can be obtained. Also, the remote observation of the JSR emission is limited in the region where the magnetic field is very strong (~ 2 R_J). Thus, a precise and global view of the energy and spatial distribution of electrons in the inner radiation belts has not yet been obtained. Understanding the distribution of such high-energy electrons is very important in clarifying their acceleration mechanism in our solar system. Variability of the Jovian diffuse X-ray emission detected by Suzaku (Ezoe et al. 2010; Numazawa et al. 2019) will give a new constraint on the acceleration mechanism of high-energy electrons, independently of what can be obtained from the radio observations. In this paper, we analyze three data sets of Jupiter observations by Suzaku in 2006, 2012, and 2014 in terms of a consistent procedure by focusing on the Jovian diffuse hard X-ray emission, and investigate reproducibility, long-term variation, and probability of the inverse-Compton scattering mechanism with comparison to an empirical magnetospheric charged particle distribution model for which we employed the Divine&Garrett model (Divine and Garrett 1983).

2 Observations and method

Suzaku (Mitsuda et al. 2007) observed Jupiter three times in its mission duration with the X-ray Imaging Spectrometer (XIS; Koyama et al. 2007) which was operated in the normal mode for every observation. The XIS consists of three front-illuminated (FI) CCDs: XIS0, 2 and 3, and one back-illuminated (BI) CCD, XIS1. Sudden anomalies caused putatively by micro-meteorite hits affect the XIS sensors. A drastic anomaly of XIS2 occurred in November 2006, and the entire sensor was lost then.

The low-Earth orbit of Suzaku and the large effective area of XIS give the lowest particle background among all X-ray CCDs which have been used for X-ray observatories, as shown in figure 5 of Mitsuda et al. (2007). The XIS FI has especially good sensitivity for spatially extended sources due to the low background in 1–5 keV where the Jovian diffuse hard X-ray emission was seen. Therefore, in this paper, we utilize only the XIS FI data for the hard diffuse emission, with the BI data used for the soft emission only.

Table 1 summarizes the parameters of the Suzaku observations. Suzaku observed Jupiter three times in February 2006, January 2012, and April 2014 with the XIS instrument with net exposure times of 159, 165, and 160 ks, respectively. Although two of these observations, in 2006 and 2014, had been reported in Ezoe et al. (2010) and Numazawa et al. (2019), whole data sets were analyzed again by a procedure renewed for this paper. Figure 1 shows the relative positions of Jupiter by fixing the positions of the Sun and the Earth (i.e., the observatory). Distances to Jupiter from the Earth are ∼5.0, 4.7, and 5.4 au, and opening angles of the line connecting Sun-Jupiter-Earth are ∼9.9°, 11.0° and 10.7°, for the observations in 2006, 2012, and 2014, respectively.

Since the Suzaku observation in 2014 was coordinated with XMM-Newton, we also use the XMM-Newton's European Photon Imaging Camera (EPIC; Turner et al. 2001; Strüder et al. 2001) with a net exposure time of 77 ks to look into the emission from Jupiter's body. The angular resolution of XMM-Newton is much better than that of Suzaku, which makes it possible to evaluate the body emission separately from the extended emission. The body emission contains strong non-thermal bremsstrahlung at $\gtrsim$2 keV from Jupiter's aurorae (Branduardi-Raymont et al. 2007a), which needs to be separated from the extended hard emission from the Suzaku data.

Jupiter moves on the sky, which requires observatories to change their pointing so that they can keep the target near the central region of their field of view. We needed 4, 5, and 14 maneuvers by taking account of motion velocities of Jupiter during the Suzaku observations in 2006, 2012, and 2014, respectively. In order to express Jupiter's events in the planet's reference frame, we also needed correction of Jupiter's position in the field of view which changed in each pointing period.

We have a correction tool, `attmove` from `XMMSAS` for XMM-Newton data (`sso_freeze` from `CIAO` for Chandra data), which is released for data analyses of solar system objects like planets and comets. However, no tools for Suzaku data can produce such correction. Therefore, we developed our original tool for data analyses of the solar system objects observed by Suzaku and used it for the Suzaku data of Jupiter, while used `attmove` for the XMM-Newton data sets

of Jupiter.

We mainly utilized `HEASoft` version 6.21 (released on April 5, 2017) and `CALDB` version 2016-06-07 for all the analyses of the Suzaku data. In addition, we used `XMMSAS` version 1.2 (xmmsas_20160201_1833-15.0.0) for the XMM-Newton data analysis. The entire Suzaku data were reprocessed after the satellite operation terminated and online-released on October 24, 2016. We employed the newly reprocessed cleaned event files with processing version 3.0.22.43 and 3.0.22.44.

Here, we briefly describe the analysis flow of the Suzaku data of Jupiter;

1. Create mosaic images in 0.2–1 (XIS BI) and 1–5 (XIS FI) keV bands from the screened event files, for which exposure corrections were made by dividing the image with exposure map generated by `xisexpmapgen` (version 2015-01-07).

2. Identify bright sources in the hard band mosaic image using `wavdetect` from `CIAO` package (version 4.11), 3XMM-DR8 Catalog (only for the 2014 observation), and/or visual detection, and exclude them from the event files to obtain contamination-free images.

3. Convert the sky coordinate of the image after the point-source exclusion into Jupiter's reference frame (JRF) coordinate.

4. Create images in the JRF coordinate in the two energy bands.

5. Make projection profiles from the JRF images, estimate the size of diffuse emission around Jupiter assuming an ellipsoidal shape, and calculate a ratio of diffuse to point-like emission (i.e., from Jupiter itself).

6. Extract spectra from a circular (for source) and a surrounding annular (for background) region, both centered at the origin of the JRF coordinate.

7. Generate the Redistribution Matrix File (RMF) for the epoch of the observation of Jupiter using `xisrmfgen` (version 2012-04-21). The Ancillary Response Files (ARFs) for the point-like and diffuse emissions are produced using `xissimarfgen` (version 2010-11-05).

8. Carry out spectral fits using `Xspec` (version 12.10.1) with the models describing Jupiter's X-ray emission and a power-law function for the Jovian diffuse hard X-ray emission. The background-subtracted spectra of all detectors (XIS FI+BI) are fitted.

Solar activity, indicated by sunspot number, showed significant variation throughout 2002–2016. During the first Suzaku observation in 2006, the activity was approaching its minimum when the 23rd solar cycle was near the end. On the other hand, in the second and third observations in 2012 and 2014, the activity was near the maximum of the 24th cycle.

3 Results

3.1 Imaging analysis

We converted all the data coordinates into JRF before we analyze the emission from Jupiter. We used Jupiter's ephemeris obtained from the Jet Propulsion Laboratory (JPL). At first, before the above-described procedure, we examined X-ray images without the coordinate correction. Figure 2 shows mosaic images of XIS BI and FI instruments in the two energy bands, 0.2–1 and 1–5 keV, respectively. The images were divided by exposure maps which were generated by the exposure map generator `xisexpmapgen`. In every image, especially in the 0.2–1 keV ones, faint trails are seen along with Jupiter's motion, indicating the detection of Jupiter's X-rays.

There were point sources in the image beside Jupiter's trail, and they are more noticeable in the 1–5 keV images. From the hard-band images, we identified a total of 27, 28, and 44 point sources in 2006, 2012, and 2014, respectively. These point sources are indicated in Figure 2 by green circles. We excluded the circular regions centered on individual sources, with a diameter equal to the beam size, i.e., the half-power diameter (HPD) of XIS ($\sim$2 arcmin) or larger. For safety, we masked these point sources for both 0.2–1 and 1–5 keV images.

We have to correct the coordinates of the event file to obtain coordinates centered at Jupiter. As we mentioned, there is no official tool for such coordinate correction, so we made it on our own. The originally developed tool can correct the coordinates by taking into account both Jupiter's motion in the sky and the satellite's orbital motion around the Earth (including the Earth's motion around the Sun). Parameters of the former were obtained from JPL HORIZON, while for the latter parameters were extracted from Suzaku orbit files packaged with the event files of the respective observations. Using this information, the tool corrects the line-of-sight direction recorded in attitude files, which are in the same package of the event files, and creates new attitude files. The event files were reprocessed by `xiscoord` (version 2009-02-28) through addressing the corrected attitude files, finally, to be converted into the JRF coordinate. This correction resulted in Jupiter being in the center of the field of view.

We created the two band images again, but in the JRF coordinate as shown in Figure 3. The point sources were removed from the event files before this step. Exposure maps can also be generated by `xisexpmapgen` with the corrected attitude files. In generating the exposure maps, the positions of the point sources, which were no more stationary in the JRF framework, were excluded using detector masks as a parameter of `xisexpmapgen`. Jupiter's movement in the 8 s interval, which is equal to Suzaku's time resolution defined by the event-by-event accumulation in CCD, corresponded to $\sim$0.007, 0.02, and 0.04 arcsec in 2006, 2012, and 2014,

respectively, as estimated from Jupiter's apparent velocity and caused a negligible image blur compared with Suzaku's HPD ($\sim$2 arcmin).

The obtained JRF images indicated different spatial extent between the soft and the hard energy bands as seen in Figure 3. The soft X-ray images are likely to agree with the point spread function (PSF) of Suzaku. On the other hand, the hard X-ray ones are surely more extended than the PSF and indicate a spatial extent. As discovered by Ezoe et al. (2010), we confirmed that the hard X-ray emission was extended around Jupiter, whereas the soft X-ray emission was concentrated on Suzaku's HPD. Since the JRF image is generated by a different method in Ezoe et al. (2010), the agreement of the image indicates that the present JRF conversion method is valid.

In order to look into the spatial distribution of the X-ray emission, we generated projection profiles along the horizontal axis as shown in Figure 4. In these plots, the data were accumulated in white dashed rectangles in Figure 3, but with a binning of 16×16 pixels without smoothing. We produced a model profile consisting of Jupiter's body (disk and aurorae) and its surroundings, with their configurations assumed to be a small circle and an ellipse, respectively. For this modeling, we utilized `xissimarfgen` by changing parameters for the shape of the X-ray emitting region. The size of the small circle describing Jupiter's body emission was fixed to be Jupiter's apparent size of 19.9, 21.1, and 18.3 arcsec for the 2006, 2012, and 2014 observations, respectively. The elliptical shape of the diffuse emission was changed in horizontal and vertical axes with a pitch of 5 arcsec. The simulated models were normalized and centered on Jupiter to be fitted with the data.

As a result, we found that the observed profile can be represented by a combination of the uniform circle with a radius of 1 R_J and a uniform elliptical emission with semi-axes of 4.2 arcmin and 1.2 arcmin corresponding to 12.6 R_J and 3.5 R_J for the 2006 observation, 5.6 arcmin and 2.4 arcmin corresponding to 15.9 R_J and 6.9 R_J for the 2012 one, and 6.4 arcmin and 2.5 arcmin corresponding to 21.0 R_J and 8.2 R_J for the 2014 one, respectively. All the hard-band emissions were surely extended over a wide region (>6 R_J). On the other hand, the soft emissions were not well-fitted by the same model and only marginally consistent with the small circular emission from Jupiter's body. The center positions of these emissions are slightly shifted from the origin of the coordinates by at most $\sim$0.5 arcmin (in 2012) corresponding to $\sim$1.4 R_J. This could not be a significant problem considering Suzaku's angular resolution and the known pointing uncertainty (Uchiyama et al. 2008).

We calculated a diffuse intensity ratio, defined as the intensity of the simulated elliptical emission (green curves in Figure 4) divided by that of the small circular emission (orange

curves), by integrating counts in the respective areas in the projection profiles. The diffuse intensity ratios (D/B ratios) were evaluated as 6.16 ± 1.78, 1.73 ± 0.24, and 1.91 ± 0.36 in 2006, 2012, and 2014, respectively.

3.2 XMM-Newton observation

Here, we describe the observed results taken in 2014 from XMM-Newton, which gives much better angular resolution ($\sim$15 arcsec in half energy width) than Suzaku and whose simultaneous data are very useful in separating Jupiter's body and diffuse components. Figure 5 shows the EPIC images in 0.2–1 and 1–5 keV, respectively. The images were reconstructed in the JRF coordinate by using `attmove` (version 1.5; from the `XMMSAS` tools) which has been officially developed to handle data of moving targets such as the solar system objects. The images were then generated by using `ESAS` tools (ESA: XMM-Newton SOC 2019). The soft X-rays contributed significantly to the auroral emission, while the hard X-rays were relatively uniform over Jupiter's body.

We did not subtract the diffuse X-ray background when producing the energy spectra because Jupiter cast a shadow to it. The residual particle background of the detector was also negligible and no more than 1% of Jupiter's flux in the band of 0.2–2 keV, while it gave significantly more contribution in higher energies. Lumb et al. (2002) reported that the EPIC particle background was flat as a function of energy and the estimated level was 0.0210 ± 0.0022 cm^{-2}s^{-1}. Considering the size of the region for which the spectrum was produced, we estimated the level to be 9.6×10^{-5} count s^{-1} which was less than 5% of the flux integrated above 2 keV. Thus, we created the EPIC source and particle background spectra using `mos-`, `pn-spectra`, `mos-` and `pn-back` (from the `ESAS` package) and subtracted the background spectra from the source spectra. These background spectra reproduce well the particle background component of each EPIC camera based on the models calibrated by the developer team. RMFs and ARFs were generated by `rmfgen` and `arfgen` from `XMMSAS` tools with the point source option, in the same manner as in Branduardi-Raymont et al. (2004); Branduardi-Raymont et al. (2007a).

Figure 6 shows the MOS and pn spectra extracted from the circular region centered on the center of Figure 5 with a radius of 24 arcsec in which the auroral emission is entirely included. The spectra were characterized by a thermal continuum with several emission lines in the lower energy band and also a continuum extending up to >5 keV. Following the analysis in Branduardi-Raymont et al. (2007a), we tried to fit a model consisting of four Gaussians along with the following three continuum components: APEC model peaked near 0.8 keV, a

thermal bremsstrahlung model in a range <0.5 keV, and a power-law function for the hard end of the spectrum. Here, we did not include an absorbing column in the model, because of the proximity of the object. The four Gaussians had center energies, 0.57, 0.65, 1.35, and 1.86 keV, which are the known values of OVII, OVIIILyα, MgXI, and SiXIII lines, respectively. Given the moderate statistical quality of the data, the center energies of the higher two lines were fixed in the spectral fits. We assumed that OVII and OVIIILyα lines were charge exchange (CX) emission from Jupiter's aurorae with the thermal bremsstrahlung model also representing unresolved CX emission, whereas MgXI and SiXIII lines were scattered solar coronal emission from Jupiter's disk which was also responsible for the thermal continuum represented by the APEC model. The power-law component represented non-thermal bremsstrahlung from keV electrons precipitating into the aurorae.

Table 2 summarizes the best-fit parameters and 90% confidence errors. The temperature of the APEC model, $\sim$0.59 keV, was consistent with the solar coronal emission (Branduardi-Raymont et al. 2007b). The temperature of the bremsstrahlung, $\sim$0.09 keV, also agreed with the results from the past XMM-Newton observations (Branduardi-Raymont et al. 2007a). The photon index Γ and normalization of the power-law component were, however, different from the past XMM-Newton observations. We estimated the 2014 flux in 2–7 keV as $(4.4 \pm 0.1) \times 10^{-14}$ erg cm^{-2} s^{-1} and compared it with that in the past observations ($\sim$2.1 $\times$ 10^{-14} erg cm^{-2} s^{-1}; after table 1 in Branduardi-Raymont et al. 2007a), which turned out to be about twice increase, even taking into account the difference of the distance to Jupiter. Such a flux change seems possible since there was a factor-of-two variation observed within several days in November 2003 from XMM-Newton (rev.0726 and 0727; Branduardi-Raymont et al. 2007a).

3.3 Spectral analysis

We analyzed the Suzaku spectrum by extracting photons from a rather wide region, in order to examine the nature of the extended emission. We used the JRF-converted event files, from which the point sources were removed, and accumulated source photons from the circle with a radius of 6 arcmin and background ones from the surrounding annulus with an outer radius of 8 arcmin using `Xselect` (version 2.4d). Both regions have the same center in the JRF coordinate. Consequently, the source region includes both Jupiter's body and diffuse emission which cannot be spatially separated by Suzaku's angular resolution (HPD of $\sim$2 arcmin). The diffuse X-ray background was subtracted using the data taken in the outer annular region. The size of Jupiter's body ($\sim$40 arcsec in diameter) was smaller than the source region and made

Jupiter's occultation of a small part of the diffuse X-ray background negligible.

Then, we generated a RMF and ARFs using `xisrmfgen` and `xissimarfgen` for each extracted spectral file, respectively. Based on the results of the profile fitting of the projected data, we prepared both point-like circular ARFs with a radius of 1 R_J and elliptically extended ARFs with the semi-axes derived above for the emission from Jupiter's body and diffuse emission, respectively. The total exposure time for each region was calculated from the pre-generated exposure maps in the JRF coordinate, and the *backscal* parameters of both the source and the background spectral files were over-written with these values. This procedure was necessary because `Xselect` did not take into account the loss of areas of the removed point-source regions in the JRF-converted event files.

The XIS spectra thus obtained are shown in Figure 7. A thermal emission accompanied by several lines can be seen in the low energy range, and an additional continuum extends up to >5 keV: this is similar to the feature seen in the EPIC spectra (Figure 6). We first tried to fit the spectra of the 2014 observation with the best-fit model from the EPIC spectral analysis by employing point-source ARFs and found a difference around the 0.5 keV line and a large excess of the hard component. Then, we allowed the center energy of the first Gaussian at 0.57 keV to be free and added a second power-law model for the diffuse emission, which uses the extended ARFs. We fixed the parameters of the first power-law component at the XMM-Newton values, which accounted for the auroral non-thermal bremsstrahlung.

Table 3 summarizes the best-fit parameters and their 90% errors. Temperatures and normalizations of the APEC and the thermal bremsstrahlung models agreed with the results of XMM-Newton's EPIC spectral fits within their errors. Fluxes of the Gaussians centered at 1.35 and 1.86 keV were consistent within their errors. The center energy of the first Gaussian in the best-fit model was 0.53 keV, which does not directly match any likely energy resulted from the CX reaction. We considered that this feature was likely to be a mixture of oxygen and nitrogen lines whose energies are 0.57 and 0.43 keV, respectively. A significant flux increase of the line-like feature at ∼0.53 keV also suggested that the condition of the CX process might have changed from that in the coordinated XMM-Newton observation. A flux of the second Gaussian at ∼0.65 keV which increased by a factor of 2.8 ± 1.5 from the coordinated XMM-Newton observation was also likely caused by the change of the CX condition. In the hard energy band, we recognize an excess from the power-law fit to XMM-Newton's EPIC data. This excess was able to be fitted by the second power-law model with Γ of $1.24^{+0.49}_{-0.56}$.

Compared with the XIS spectrum in 2014, the CX lines in 0.5–0.7 keV of the XIS spectrum in 2012 are less significant. However, the 2012 spectrum shows a thermal emission

peaked around 0.8–0.9 keV with several emission lines in 1–2 keV, and also a hard continuum extending up to >5 keV as the 2014 spectrum does. Emission below 0.5 keV was likely to be a CX component. The spectral model consists of the following components: four Gaussians, an APEC model peaked near 0.8 keV, a thermal bremsstrahlung model in the range <0.5 keV, using the point-like ARFs, and a power-law model for the hard band using the extended ARFs. The last component represented not only the diffuse emission but also the auroral non-thermal emission which was not able to be separated. Because of the statistical quality, the four Gaussians had their center energies fixed at 0.57, 0.65, 1.35, and 1.86 keV in the same way as for the XMM-Newton EPIC data analysis. The former two lines probably represented the CX emission of OVII and OVIIILyα from Jupiter's aurorae, whereas the latter two were MgXI and SiXIII lines in the scattered solar coronal emission from Jupiter's disk.

The whole spectrum in 2012 was able to be reproduced with similar parameters as those in 2014. The temperature of the APEC model was 0.64 keV and corresponded well with the solar coronal temperature. The APEC model showed almost the same normalization as for the 2014 Suzaku XIS spectrum. The bremsstrahlung temperature was also consistent with the results of the 2014 Suzaku XIS and XMM-Newton EPIC observations. The power-law slope was quite flat with $\Gamma = 0.87^{+0.30}_{-0.32}$ implying non-thermal emission as in the 2014 case.

The soft-band emission in the 2006 spectrum was slightly weaker than those in the 2014 and 2012 ones, as indicated by the image analysis (Figure 3). In contrast, the hard band intensity was similar to those in the other observations. The fitted model was almost the same as the 2012 one, but the bremsstrahlung was replaced by a Gaussian function with a center energy 0.25 keV. This was because the spectrum did not show continuum emission below <0.5 keV. We fitted with all the line energies fixed at 0.25, 0.57, 0.65, 1.35, and 1.86 keV and determined the APEC temperature. Then, we allowed the center energies of the former three lines to be free and obtained the best-fit model.

The temperature of the APEC model in the 2006 observation was $0.73^{+0.13}_{-0.17}$ keV which was also consistent with the solar coronal temperature. The normalization of the APEC model was lower than the 2014 and 2012 levels, likely to correlate with the decrease of the solar activity. The line energies were $0.25^{+0.01}_{-0.03}$, 0.55 ± 0.02, and 0.68 ± 0.02 keV, which presumably correspond to line complexes from CVI, ionized Mg, Si, and S, OVII, and OVIII ions, respectively. The power-law slope $\Gamma = 0.65^{+0.36}_{-0.40}$, again, implies non-thermal emission.

Finally, we calculated fluxes and estimated luminosities in 0.2–1 and 1–5 keV from the respective best-fit model. The fluxes in 0.2–1 and 1–5 keV in 2014 were calculated as $(25.5 \pm 1.6) \times 10^{-14}$ and $(13.2 \pm 1.1) \times 10^{-14}$ erg cm^{-2} s^{-1}, respectively. Then, the luminosities

were corrected for the distance to Jupiter at the observed epoch and were estimated as $(21.0\pm 1.3)\times 10^{15}$ and $(10.8\pm 0.9)\times 10^{15}$ erg s^{-1} for 0.2–1 and 1–5 keV, respectively. As for the two hard components, which were Jupiter's body and diffuse emission, the luminosities in 1–5 keV were separately obtained as $(4.5\pm 0.3)\times 10^{15}$ and $(6.3\pm 0.9)\times 10^{15}$ erg s^{-1}, respectively. We also calculated the luminosity ratio, namely the diffuse luminosity divided by that of Jupiter's body, as 1.41 ± 0.22. This value was consistent with the D/B ratio in 2014 (1.91 ± 0.36) obtained for the projection profile within each error.

Based on this, we used the D/B ratios from the projection profiles to estimate the separate luminosities from Jupiter's body and diffuse emission in the other observations in 2006 and 2012 for which no coordinated observation with XMM-Newton was carried out. The fluxes and luminosities obtained from the entire three Suzaku observations are listed in Table 4. In this table, we used the D/B ratios, 6.16 ± 1.78 and 1.73 ± 0.24 for 2006 and 2012, respectively, from the projection profiles, and estimated the individual contributions from Jupiter's body and diffuse emission in the 1–5 keV band. By combining the imaging and spectral analyses (and based on the coordinated observation with XMM-Newton), they were obtained separately for the first time in our knowledge.

Finally, we plotted a variation of each of the obtained X-ray luminosity values and compared them to that of the solar activity as shown in Figure 8. In this figure, we described the result of the 2006 observation as unity and calculated ratios for the other epochs to it. As the solar activity increased from 2006 to 2012 and 2014, the soft and hard luminosities of the emission from Jupiter's body clearly increased by a factor of 2–5. The soft X-rays from Jupiter's body consist of the solar X-ray scattering and the CX interaction with this planet's atmosphere of heavy ions which originate in not only IPT or the Jovian magnetosphere but also in the solar wind. Thus, we considered that the increase was likely to depend on the solar activity to a certain degree. The hard X-rays from Jupiter's body consist of the bremsstrahlung by energetic keV electrons in the magnetosphere. Branduardi-Raymont et al. (2007a) have implied that the hard bremsstrahlung may be driven by the solar activity. We thought that our results of Jupiter's body emission also supported this possibility.

In contrast, the hard luminosity of the diffuse emission was relatively stable within 20–30% at most, and did not simply depend on the solar activity. This variability was marginally consistent with that of the JSR emission which originates from high-energy electrons with an energy of a several MeV and shows a tendency to be out of sync with the solar activity after 1994 when Comet Shoemaker-Levy 9 impacted on Jupiter (Bolton et al. 2002; Santos-Costa et al. 2008; Han et al. 2018). In the following section, we discuss the diffuse hard X-ray emission

referring to the possibility of the inverse-Compton scattering hypothesis proposed by Ezoe et al. (2010).

4 Discussion

As already mentioned, Ezoe et al. (2010) have proposed the inverse-Compton scattering hypothesis in which ultra-relativistic electrons with an energy of $\lesssim 50$ MeV observed by Cassini spacecraft at 1.4 R_J (Bolton et al. 2002) produce an X-ray continuum extended around Jupiter. The inverse-Compton scattering is an important process in producing high-energy photons in diverse astrophysical settings (chapter 7 in Rybicki and Lightman 1979). In the hypothesis, solar visible photons are scattered by magnetospheric high-energy electrons and are energized into X-ray bands, so that characteristic energy of the scattered photons is given by equation 7.25 in Rybicki and Lightman (1979) as,

$$\sim 3 \text{ keV} \left(\frac{E_{\text{ph}}}{1.4 \text{ eV}}\right)\left(\frac{E_{\text{e}}}{20 \text{ MeV}}\right)^2, \tag{1}$$

where E_{ph} and E_{e} are the energies of the solar photons and the relativistic electrons before the scattering process. The Thomson cross section is applicable as the scattering cross section in this process on condition that the electrons are relativistic.

This mechanism does not produce any line emission, which is consistent with the observed XIS spectra, and also can explain the anisotropic feature of the diffuse emission along a horizontal axis. At an outer region ($>$ several R_J), such $\lesssim 50$ MeV electrons have not been directly observed yet, but their presence may be examined through empirical models of particle distribution in the Jovian magnetosphere (e.g., Divine and Garrett 1983). Ezoe et al. (2010) explained that the inverse-Compton hypothesis has an open issue about the low density of such high-energy magnetospheric electrons based on their estimation from the empirical model by Divine and Garrett (1983) (D&G model).

The D&G model is based on past *in-situ* measurements and describes the spatial distribution of charged particles around Jupiter. Then, we employed this model and quantitatively examined the possibility of inverse-Compton scattering. Although there are other models of the distribution of charged particles in the Jovian magnetosphere, we will use the D&G model because the model is most "comprehensive". The D&G model is based on the data collected during the Pioneer and Voyager flybys of Jupiter combined with earth-based observations and is the only global model applicable from the inner to outer magnetosphere up to 16 R_J. The model also covers a wide range of electron energy higher than 0.06 MeV. This was the first attempt of the evaluation of inverse-Compton scattering distribution based on the model of

charged particle distribution in the Jovian magnetosphere. We calculated the expected X-ray luminosity and spectrum and compared them with the observed results from the Suzaku observations.

The X-ray emission produced in the inverse-Compton scattering by the ultra-relativistic electrons can be calculated in our code. The calculation is carried out with a pitch of 2 R_J over a spatial range of <16 R_J in equatorial X- and Y-directions and <10 R_J in vertical Z-direction. The covered range of electron energy is from 0.06 to 50 MeV. The actual code employed a python package `naima` (version 0.8.4; Zabalza 2016) to yield an X-ray differential flux or spectral energy distribution at a given position by taking spatial and spectral distributions of electrons given by the D&G model. We assume that the solar visible photons, which are subject to scattering by the electrons in this process, form a black body distribution with a temperature of 5780 K and that the distance from the photon source is 5.2 au. They corresponded to the temperature of the Sun's photosphere and the average orbital radius of Jupiter, respectively. We used 170° as a scattering angle between the solar photons and the scattered X-ray photons, referring to the Sun-Jupiter-Observer angle of ∼10° in the Suzaku observations.

Figure 9 shows the calculated results. The 1–5 keV X-ray features calculated from such electron distributions in a certain meridian surface are shown in the top two panels. Here, the photon index (the left panel) was estimated by fitting a power-law function to a calculated photon spectrum at each location. In terms of spatial distribution, the density distribution of the higher electrons seemed to be reflected in the X-ray power (the right panel). We, then, conducted a three-dimensional calculation over the magnetosphere assumed by the D&G model. The resultant images integrated along the direction of a line of sight are shown as the bottom two panels in Figure 9. We confirmed again that the integrated density distribution of the high energy electrons is surely reflected in the integrated X-ray power distribution.

The total inverse-Compton luminosity based on the D&G model was calculated as ∼ 5.7×10^{13} erg s^{-1}, which is ∼100 times lower than the observed values by Suzaku (see Table 4). We also estimated the count rate of the inverse-Compton X-rays using the XIS FI effective area 330 cm^2 at 1.5 keV for each position and generated its projection profile along the horizontal axis. This can be compared with the observed profile. The results are shown in Figure 10. Results of fitting an elliptical shape to the observed projection profiles are shown in Figure 4, and are reproduced here as the observed count rates. The difference between the D&G model estimation and the observed profiles is relatively small with a factor of <10 in the inner region (<10 R_J). In contrast, it becomes significantly larger to factors of 10–100 in the outer region (>10 R_J). The model deficiency in the outer region is the main cause of the discrepancy with the

observed results, with the proviso that it may be somewhat mitigated by considering the CXB contamination comparable to the diffuse emission in such an outer region (see the background levels in Figure 4) and the electron pitch angle which efficiently acts on the inverse-Compton scattering but is ignored in the model.

Bolton et al. (2001) and Bagenal et al. (2004) suggested that the D&G model probably underestimated the actual particle density in the Jovian magnetosphere by a factor of 5–10, based on a comparison of the D&G model with radio observations. The radio observations measured the Jovian synchrotron radio emission, so the data were limited in the inner region within several R_J where Jupiter's magnetic field is strong. In this regard, our result which extends further out from the inner region is consistent with their suggestion. On the other hand, our result for the outer region has no comparable observations which provide a meaningful constraint on the particle distribution. Therefore, we have given the first observational result indicating that the D&G model (especially for higher energy electrons) underestimates the electron density by a factor of 10–100 in the distant region, where no data of such energetic particles have been obtained by *in-situ* spacecrafts.

We, additionally, estimated a photon index of the inverse-Compton scattering based on the D&G model by fitting a power-law function to the spectrum in each radial position and found it to be 1.6–2.0 (lower left in Figure 9). The photon index expected from the D&G-model is slightly steeper as compared with the observed values. Thus, we also conclude that the D&G model underestimates preferentially the higher energy particles.

The most likely origin of the diffuse hard X-ray emission around Jupiter is the inverse-Compton emission from the magnetosphere. In this case, electrons with an energy of about 50 MeV are accelerated in a wide region in Jupiter's magnetosphere. Quantitative comparison with the D&G model showed that the electron density predicted by the model was unable to explain the observed hard X-ray luminosity by a factor of $\lesssim$100. This raises a possibility that the particle acceleration in the middle magnetosphere is more efficient as suggested by Horne et al. (2008), e.g., via the whistler-mode wave-particle interactions (Miyoshi et al. 2003), than the previous picture in a distant region as far as 15–20 R_J from Jupiter. The chorus waves in the Jovian magnetosphere had been often observed in a region between 6 to 15 R_J by the Galileo *in-situ* measurements, but the detection had been constrained along the spacecraft trajectory (e.g., figure 1 in Menietti et al. 2016). It is possible that the chorus waves are more widely distributed or other unrecognized processes exist in such distant positions. These results re-emphasize the necessity that the D&G model should be improved especially at such distant positions.

5 Summary

Suzaku discovered a diffuse hard X-ray emission around Jupiter in 2006 (Ezoe et al. 2010). A scenario that the inverse-Compton scattering process between solar visible light and ultra-relativistic ($\lesssim$50 MeV) electrons in the Jovian magnetosphere produces the diffuse emission has been suggested. Numazawa et al. (2019) confirmed the discovery and discussed a solar dependence of the diffuse emission from the 2006 and 2014 observations when the solar activity was going toward its minimum in the 23rd cycle and reached at maximum in the 24th cycle, respectively.

In this paper, we have investigated the X-ray emission in the vicinity of Jupiter using the Suzaku observations, combined with a coordinated XMM-Newton observation. In order to verify the emission mechanism and variation of the hard X-ray emission, we looked into all three Suzaku XIS data sets from observations of Jupiter in 2006, 2012, and 2014, together with XMM-Newton EPIC data coordinately taken in 2014. Here, to keep the consistency of the analysis, we addressed the 2006 and 2014 data again using a uniform procedure. Consequently, we have obtained the following results and their subsequent interpretation.

- The successively corrected images in Jupiter's reference frame in two energy bands (0.2–1 and 1–5 keV), without any contamination from point sources other than Jupiter, showed the hard-band X-ray emission to be extended around Jupiter for all the three Suzaku observations in 2006, 2012, and 2014.
- We examined the spatial extent of the diffuse emission from projection profiles of count rates along the horizontal directions, after accumulation of data in a rectangular (15 arcmin $\times$ 6 arcmin) region around Jupiter. Assuming point-like emission from Jupiter's body and elliptical emission around it, the projection profile in the hard band was well-fitted by the model combining them, whereas the soft X-ray emission was fitted by only the point-like emission. This allowed us to calculate the intensity ratio of the elliptical emission to the point-like emission (D/B ratio).
- The background-subtracted spectra were fitted with a model composed of APEC, thermal bremsstrahlung, Gaussian functions, and a power-law function, which corresponded to the solar X-rays, charge exchange emission below 0.4 keV and around 0.5–0.7 keV, and the diffuse hard component. We added, only in the 2014 spectrum, another power-law function describing the non-thermal bremsstrahlung in Jupiter's aurorae with consistency to an independent fit to the XMM-Newton EPIC spectrum from a coordinated observation which showed no diffuse hard emission because of a lack of sensitivity for such diffuse emission. This spectral

analysis for the 2014 data provided a key result that the flux ratio of these two power-law functions in 1–5 keV was consistent with the D/B ratio obtained from the projection profile within their errors.

- The X-ray luminosity in the hard band could be separated into two components, namely emission from Jupiter's body and the diffuse emission, using the D/B ratios even in 2006 and 2012. The luminosity of the diffuse emission remained stationary with no clear correlation with the variability of the solar activity. In contrast, Jupiter's body showed variability corresponding to the solar activity and indicated a relatively large enhancement in 2012 and 2014 by a factor of 2–5 from the level in 2006.

- The X-ray luminosity of the inverse-Compton scattering calculated from the Divine&Garrett empirical magnetospheric charged particle distribution model (Divine and Garrett 1983) is insufficient to match the observations by a factor of $\sim$100 in the entire region calculated here (<16 R_J). However, the projection profile of count rates indicated that the D&G model underestimated the electron density by factors of <10 in the inner region (<10 R_J), which was consistent with the result from past observations of Jovian synchrotron radio (JSR) emission (Bolton et al. 2001). On the other hand, the majority of the discrepancy of the electron density was contributed in the outer region (>10 R_J) where we have a limitation of range in the D&G model and no comparable JSR observation.

These results raise the issue that more data are required in future, because observations of the Jovian diffuse hard X-ray emission can globally monitor the origin and behavior of ultra-relativistic electrons in the Jovian magnetosphere. There are no satisfactory models of the Jovian magnetospherical particle distribution. The D&G model employed here underestimates the actual electron density as mentioned above (Bolton et al. 2001; Bagenal et al. 2004), whereas other physical (Santos-Costa and Bolton 2008) and empirical (Garret et al. 2005) models predict rather higher integral fluxes than observed, by up to a factor of $\sim$5, than observed from the Juno *in-situ* measurements at high latitudes inside Io's orbit (Becker et al. 2017). The observations of the Jovian diffuse hard X-ray emission probably help such particle distribution models to be improved, which leads to the proper design of spacecrafts in Jupiter's radiation environment. Monitoring of the energetic electrons in the Jupiter system will give important clues in clarifying the mechanism of particle acceleration in the Jovian magnetosphere, whose knowledge would be further connected to our understanding of the particle acceleration phenomena occurring in stars, supernova remnants, black hole systems, and clusters of galaxies in the universe.

We expect that useful data will be obtained not only from X-ray observatories which are

planned for launch soon such as XRISM (Tashiro et al. 2018) and Athena (Barret et al. 2020), but also from Jupiter *in-situ* probe missions carrying small X-ray instruments (e.g., JUXTA; Ezoe et al. 2013). Such a probe mission can obtain data with high spatial resolution and high statistics since it can make observations very close to Jupiter compared with those from the Earth's neighborhood. We also believe that the results described in this paper will be quite valuable for future missions of Jupiter exploration planned after the 2030s.

Table 1. Specifications of the Suzaku observations of Jupiter. Parameters are taken from NASA's Jet Propulsion Laboratory HORIZONS Web-Interface.

Date	2006 Feb. 24–28	2012 Jan. 3–13	2014 Apr. 15–21 / 15–16&20[†]
Position (R.A., Decl.)	$\sim$(226.6, $-$16.2)	$\sim$(28.9, 10.6)	$\sim$(104.2, 23.1)
Exposure (ks)	159	165	160 / 77[†]
Distance (au)	5.0	4.7	5.4
Apparent radius (arcsec)	19.9	21.1	18.3
Angle* ($^\circ$)	9.9	11.0	10.7
Motion velocity (arcsec h^{-1})	3.3	7.3	19.9
Maneuver	4	5	14 / 2[†]
Observation ID	401001010	506006010	508023010
	401001020	506006020	508023020
	401001030	506006030	508023030
	401001040	506006040	508023040
		506006050	508023050
			508023060
			508023070
			508023080
			508023090
			508023100
			508023110
			508023120
			508023130
			508023140
			rev.2628[†]
			rev.2630[†]

* Sun-Jupiter-Earth angle.

[†] Parameters for the coordinated XMM-Newton observation.

Table 2. Best-fit parameters (and their 90% confidence errors) for the XMM-Newton MOS (0.4–8 keV) and pn (0.2–2 keV) spectra of a point-like emission region in 2014.

APEC[*]	kT[†]	Norm.[‡]
	$0.59^{+0.02}_{-0.02}$	$27.1^{+1.2}_{-1.4}$
Gaussian[§]	Line energy[‖]	Flux[#]
	$0.57^{+0.002}_{-0.01}$	$17.3^{+2.1}_{-2.2}$
	$0.66^{+0.01}_{-0.01}$	$6.8^{+2.1}_{-1.4}$
	1.35 (fixed)	$1.0^{+0.3}_{-0.3}$
	1.86 (fixed)	$0.5^{+0.3}_{-0.3}$
Bremss.	kT[†]	Norm.[‡]
	$0.09^{+0.02}_{-0.02}$	$1562.5^{+1585.2}_{-792.8}$
Power-law	Γ (Photon index)	Norm.[‡]
	$0.85^{+0.19}_{-0.25}$	$4.3^{+1.3}_{-1.2}$
χ^2/d.o.f[**]	118.25 / 79	

[*] APEC abundance parameter is set by `aspl` (Asplund et al. 2009).

[†] APEC or bremsstrahlung temperature in keV.

[‡] Normalization in units of 10^6 photons cm^{-2} s^{-1} keV^{-1}.

[§] The widths of Gaussians are fixed at 0.01 keV in the fits.

[‖] Energy of the emission line features in keV.

[#] Total flux in the line in units of 10^6 photons cm^{-2} s^{-1}.

[**] χ^2 value and degrees of freedom.

Table 3. Best-fit parameters (and their 90% confidence errors) for the Suzaku XIS FI (0.7–7, 0.75–7, and 0.65–9 keV for 2006, 2012, and 2014, respectively) and BI (0.2–2, 0.2–3, and 0.2–3.5 keV for 2006, 2012, and 2014, respectively) spectra of each extended region.

Body		2006		2012		2014	
APEC*	$kT^\dagger$	Norm.‡	$kT^\dagger$	Norm.‡	$kT^\dagger$	Norm.‡	
	$0.73^{+0.13}_{-0.17}$	$15.4^{+4.0}_{-4.2}$	$0.64^{+0.09}_{-0.08}$	$29.5^{+4.9}_{-5.0}$	$0.53^{+0.1}_{-0.2}$	$30.7^{+27.2}_{-3.8}$	
Gaussian§	Line energy$^\parallel$	Flux$^\#$	Line energy$^\parallel$	Flux$^\#$	Line energy$^\parallel$	Flux$^\#$	
	$0.25^{+0.01}_{-0.03}$	$96.9^{+264.4}_{-36.8}$	0.57 (fixed)	$28.1^{+16.0}_{-16.0}$	$0.53^{+0.01}_{-0.01}$	$46.7^{+57.9}_{-16.2}$	
	$0.55^{+0.02}_{-0.02}$	$24.7^{+23.8}_{-15.7}$	0.65 (fixed)	$15.2^{+7.4}_{-7.4}$	$0.65^{+0.02}_{-0.03}$	$19.1^{+9.7}_{-8.3}$	
	$0.68^{+0.02}_{-0.02}$	$11.9^{+6.7}_{-6.4}$	1.35 (fixed)	$0.6^{+1.0}_{-0.6}$	1.35 (fixed)	$1.1^{+1.7}_{-1.1}$	
	1.35 (fixed)	$0.7^{+1.5}_{-0.7}$	1.86 (fixed)	$0.6^{+1.2}_{-0.6}$	1.86 (fixed)	$2.2^{+1.7}_{-1.5}$	
	1.86 (fixed)	$1.1^{+1.4}_{-1.1}$					
Bremss.	$kT^\dagger$	Norm.‡	$kT^\dagger$	Norm.‡	$kT^\dagger$	Norm.‡	
	—	—	$0.09^{+0.04}_{-0.03}$	$2794.6^{+12618.8}_{-1717.1}$	$0.08^{+0.10}_{-0.05}$	$1927.9^{+17870.1}_{-1608.0}$	
Power-law	Γ (Photon index)	Norm.‡	Γ (Photon index)	Norm.‡	Γ (Photon index)	Norm.‡	
	—	—	—	—	0.85 (fixed)	4.3 (fixed)	
Diffuse Power-law	Γ (Photon index)	Norm.‡	Γ (Photon index)	Norm.‡	Γ (Photon index)	Norm.‡	
	$0.65^{+0.36}_{-0.40}$	$8.4^{+5.4}_{-3.9}$	$0.87^{+0.30}_{-0.32}$	$12.4^{+5.6}_{-4.5}$	$1.24^{+0.49}_{-0.56}$	$15.3^{+10.9}_{-8.2}$	
χ^2/d.o.f**	29.41 / 20		17.71 / 29		28.84 / 26		

* APEC abundance parameter is set by `aspl` (Asplund et al. 2009).

† APEC or bremsstrahlung temperature in keV.

‡ Normalization in units of 10^6 photons cm^{-2} s^{-1} keV^{-1}.

§ The widths of Gaussians are fixed at 0.01 keV in the fits.

‖ Energy of the emission line features in keV.

Total flux in the line in units of 10^6 photons cm^{-2} s^{-1}.

** χ^2 value and degrees of freedom.

Table 4. X-ray fluxes and luminosities of Jupiter's X-rays observed by *Suzaku* in 2006, 2012, and 2014.

Errors are 68% confidence range.

Obs. year	Energy range[*]	Flux[†]	Luminosity[‡]
2006	0.2–1.0	11.1 ± 0.9	7.8 ± 0.7
	1.0–5.0	9.3 ± 0.7	6.5 ± 0.5
	Body[§]	—	0.9 ± 0.2
	Diffuse[§]	—	5.6 ± 2.2
2012	0.2–1.0	29.3 ± 1.5	18.2 ± 0.9
	1.0–5.0	11.1 ± 0.8	6.9 ± 0.5
	Body[§]	—	2.5 ± 0.3
	Diffuse[§]	—	4.4 ± 0.8
2014	0.2–1.0	25.5 ± 1.6	21.0 ± 1.3
	1.0–5.0	13.2 ± 1.1	10.8 ± 0.9
	Body[∥]	5.5 ± 0.4	4.5 ± 0.3
	Diffuse[∥]	7.7 ± 1.1	6.3 ± 0.9

[*] Energy in units of keV.

[†] Flux in units of 10^{-14} erg cm^{-2} s^{-1}.

[‡] Luminosity in units of 10^{15} erg s^{-1}, calculated with a distance to Jupiter listed in Table 1.

[§] Calculated by using the D/B ratio resulted in analyses of projection profiles.

[∥] Calculated by using each model parameter of spectral fits to the Suzaku XIS data combining the XMM-Newton EPIC data.

Acknowledgments

References

Asplund, M., Grevesse, N., Sauval, A.J., Scott, P. 2009, ARA&A, 47, 481–522

Bagenal, F., Dowling, T.E., McKinnon, W.B. (Eds.) 2004, *Jupiter: the planet, satellites, and magnetosphere*, Cambridge planetary science., Cambridge University Press, Cambridge, UK; New York

Barret, D., Decourchelle, A., Fabian, A., Guainazzi, M., Nandra, K., Smith, R., Herder, J.-W. den 2020,Astronomische Nachrichten 341, 224–235

Becker, H.N., et al. 2017 Geophysical Research Letters 44, 4481–4488

Bhardwaj, A., et al. 2007, Planet. Space Sci., 55, 1135–1189

Bolton, S.J., et al. 2001,Geophysical Research Letters, 28, 907–910

Bolton, S.J., et al. 2002, Nature, 415, 987–991

Branduardi-Raymont, G., Elsner, R.F., Gladstone, G.R., Ramsay, G., Rodriguez, P., Soria, R., Waite, J.H. 2004, A&A, 424, 331–337

Branduardi-Raymont, G., et al. 2007, A&A, 463, 761–774

Branduardi-Raymont, G., et al. 2007, Planet. Space Sci., 55, 1126–1134

Branduardi-Raymont, G., Elsner, R.F., Galand, M., Grodent, D., Cravens, T.E., Ford, P., Gladstone, G.R., Waite, J.H. 2008,J. Geophys. Res.: Space Physics, 113

Bunce, E.J., Cowley, S.W.H., Yeoman, T.K. 2004, J. Geophys. Res.: Space Physics, 109

Cravens, T.E., Howell, E., Waite Jr., J.H., and Gladstone, G.R. 1995, Journal of Geophysical Research: Space Physics, 100, A9, 17153-17161

Divine, N., Garrett, H.B. 1983,J. Geophys. Res., 88, 6889

Elsner, R.F., et al. 2005,J. Geophys. Res.: Space Physics, 110

ESA: XMM-Newton SOC 2019, XMM-Newton Users Handbook (No. Issue 2.17)

Ezoe, Y., Ishikawa, K., Ohashi, T., Miyoshi, Y., Terada, N., Uchiyama, Y., & Negoro, H. 2010, ApJ, 709, L178–L182

Ezoe, Y., et al. 2013,Advances in Space Research 51, 1605–1621

Garrett, H.B., Levin, S.M., Bolton, S.J., Evans, R.W., Bhattacharya, B. 2005Geophysical Research Letters 32

Gladstone, G.R., et al. 2002,Nature, 415, 1000–1003

Han, S., Murakami, G., Kita, H., Tsuchiya, F., Tao, C., Misawa, H., Yamazaki, A., Nakamura, M. 2018, J. Geophys. Res.: Space Physics, 123, 9508–9516

Horanyi, M., Cravens, T.E., Waite, J.H. 1988,J. Geophys. Res., 93, 7251

Horne, R.B., Thorne, R.M., Glauert, S.A., Douglas Menietti, J., Shprits, Y.Y., Gurnett, D.A. 2008,

Nature Phys., 4, 301–304

Houston, S.J., Cravens, T.E.,Schultz, D. R., Gharibnejad, H., Dunn, W.R., Haggerty, D.K., Rymer, A.M., Mauk, B.H., and Ozak, N. 2020, Journal of Geophysical Research: Space Physics, 125, 2, e2019JA027007

Kharchenko, V., Bhardwaj, A., Dalgarno, A., Schultz, D.R., Stancil, P.C. 2008,J. Geophys. Res.: Space Physics, 113

Koyama, K., et al. 2007, PASJ, 59, S23–S33

Lumb, D. 2002, EPIC BACKGROUND FILES XMM-SOC-CAL-TN-0016 issue 2.0 15.

Maurellis, A.N., Cravens, T.E., Gladstone, G.R. and Waite, J.H., and Acton, L.W. 2000, Geophysical Research Letters, 27, 9, 1339-1342

Menietti, J.D., et al. 2016, J. Geophys. Res.: Space Physics, 121, 9758–9770

Metzger, A.E., Gilman, D.A., Luthey, J.L., Hurley, K.C., Schnopper, H.W., Seward, F.D., & Sullivan, J.D. 1983, J. Geophys. Res. 88, 7731

Mitsuda, K., et al. 2007, PASJ, 59, S1–S7

Miyoshi, Y., Misawa, H., Morioka, A., Kondo, T., Koyama, Y., Nakajima, J. 1999Geophys. Res. Lett., 26, 9–12

Miyoshi, Y., Morioka, A., Misawa, H., Obara, T., Nagai, T., Kasahara, Y. 2003J. Geophys. Res.: Space Physics, 108(A1), 1004

Numazawa, M., et al. 2019, PASJ, 71, 93(1–9)

Rybicki, George B. and Lightman, Alan P., 1979, "Radiative Processes in Astrophysics", Wiley, Weinheim

Santos-Costa, D., Bolton, S.J., Thorne, R.M., Miyoshi, Y., Levin, S.M. 2008, J. Geophys. Res.: Space Physics, 113, A01204

Santos-Costa, D., Bolton, S.J. 2008Planetary and Space Science 56, 326–345

Singhal, R.P., Chakravarty, S.C., Bhardwaj, A., Prasad, B. 1992,J. Geophys. Res.: Planets, 97, 18245–18256

Strüder, L., et al. 2001, A&A, 365, L18–L26

Tashiro, M., et al. 2018,Presented at the Space Telescopes and Instrumentation 2018: Ultraviolet to Gamma Ray, International Society for Optics and Photonics, p. 1069922

The SunPy Community, et al. 2015,Comput. Sci. Disc. 8, 014009

Turner, M.J.L., et al. 2001, A&A, 365, L27–L35

Uchiyama, Y., et al. 2008, PASJ, 60, S35–S41

Waite Jr., J.H., Gladstone, G.R., Lewis, W.S., Drossart, P., Cravens, T.E., Maurellis, A.N., Mauk, B.H., Miller, S. 1997,Science, 276, 104–108

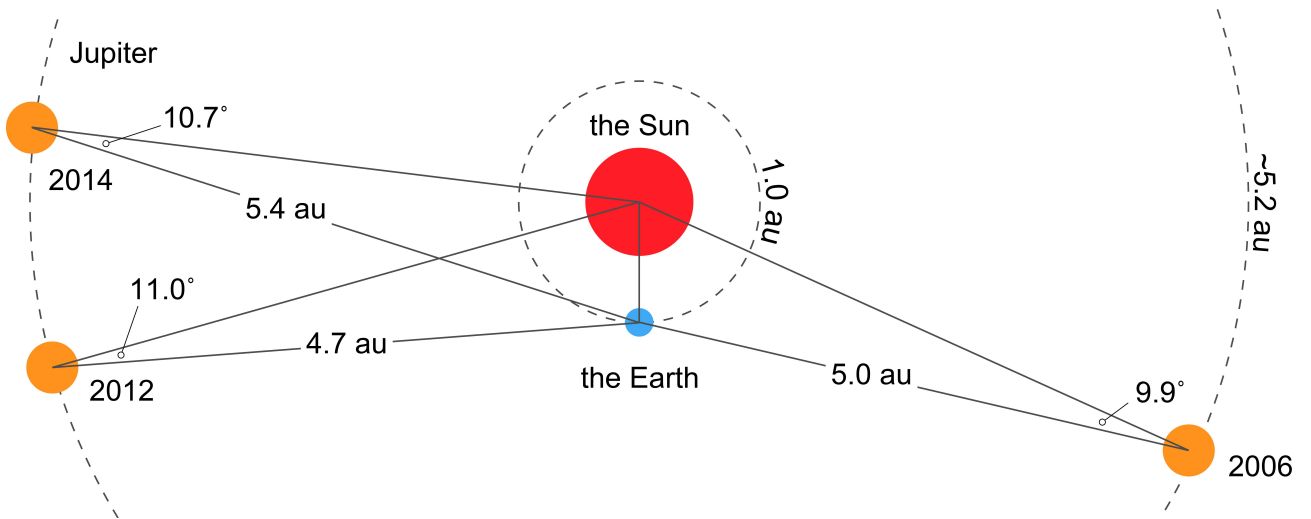Zabalza, V. 2016, Proceedings of The 34th International Cosmic Ray Conference - PoS(ICRC2015), p.922

Fig. 1. Relative positions of Jupiter with respect to the Sun and the Earth.
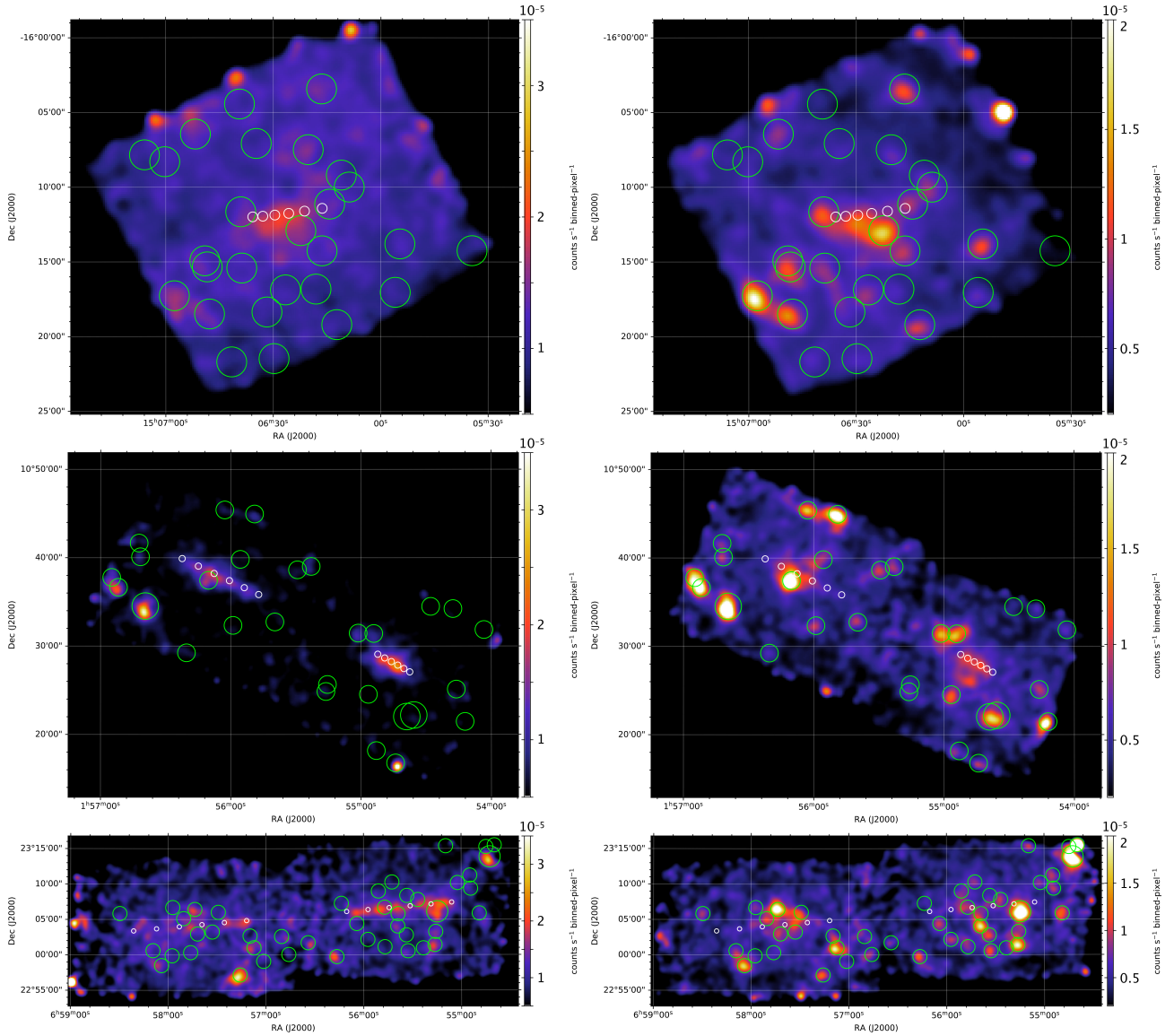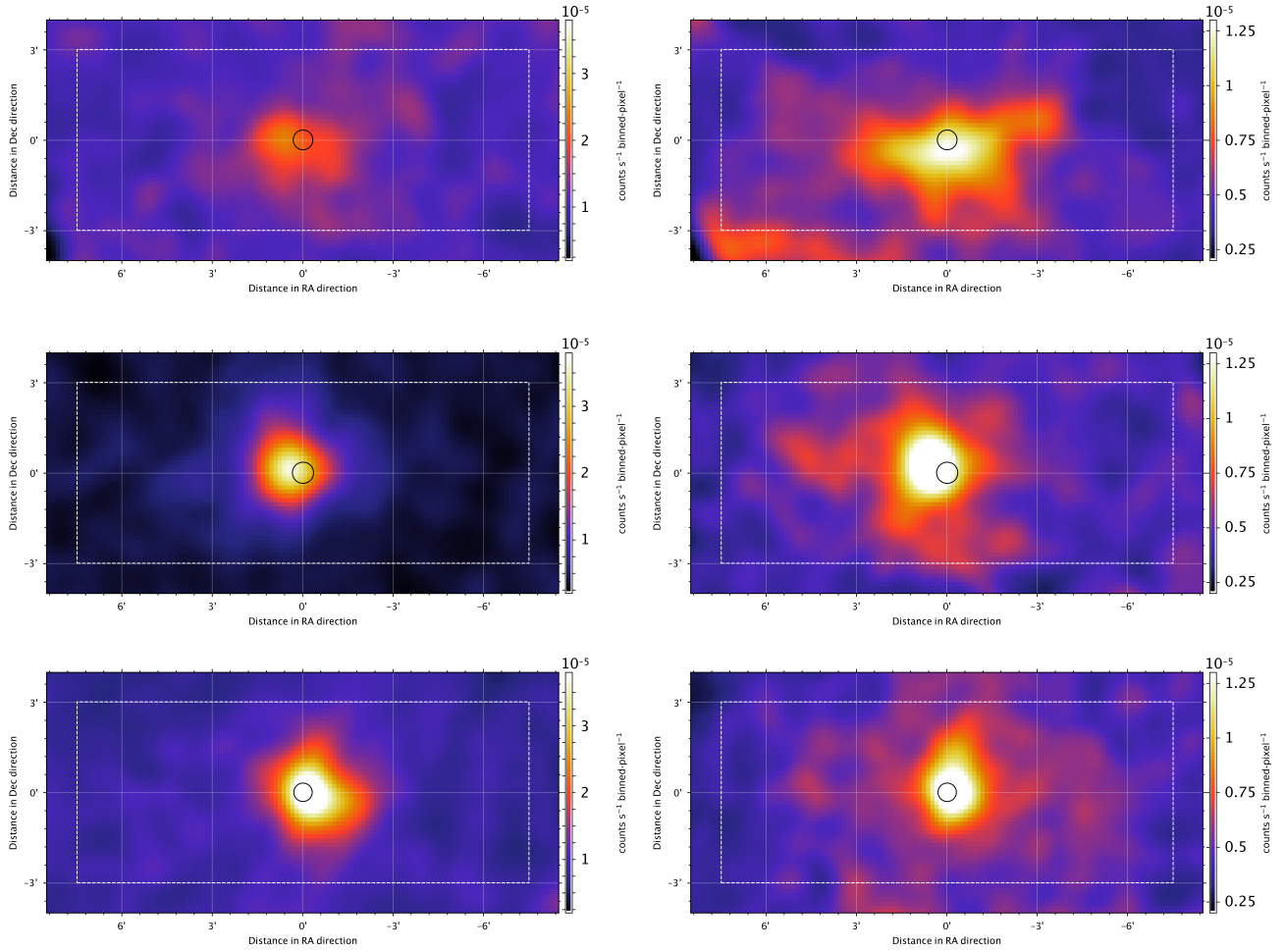
Fig. 2. Suzaku XIS mosaic images of the vicinity of Jupiter observed in 2006 (top), 2012 (middle), and 2014 (bottom) in 0.2–1 keV (BI; left) and 1–5 keV (FI; right), displayed on the J2000.0 coordinates. Exposures are corrected so that the unit is counts s^{-1} binned-pixel^{-1}. For clarity, the images are binned in 8 × 8 original pixels and smoothed by a Gaussian with a kernel size of 3 × 3 binned-pixels. White circles show the size and trajectory of Jupiter during the observations. Green circles indicate point sources that are omitted when we superpose the images in Jupiter's reference frame.

Fig. 3. Suzaku XIS images of Jupiter observed in 2006 (top), 2012 (middle), and 2014 (bottom) in 0.2–1 keV (BI; left) and 1–5 keV (FI; right), after correcting for Jupiter's ephemeris and Suzaku's orbital motion. The images are exposure-corrected, binned, and smoothed in the same way as in Figure 2. Black circles show the size and position of Jupiter. White dashed rectangles show the region used for projection profiles, with a size of 15 arcmin × 6 arcmin.
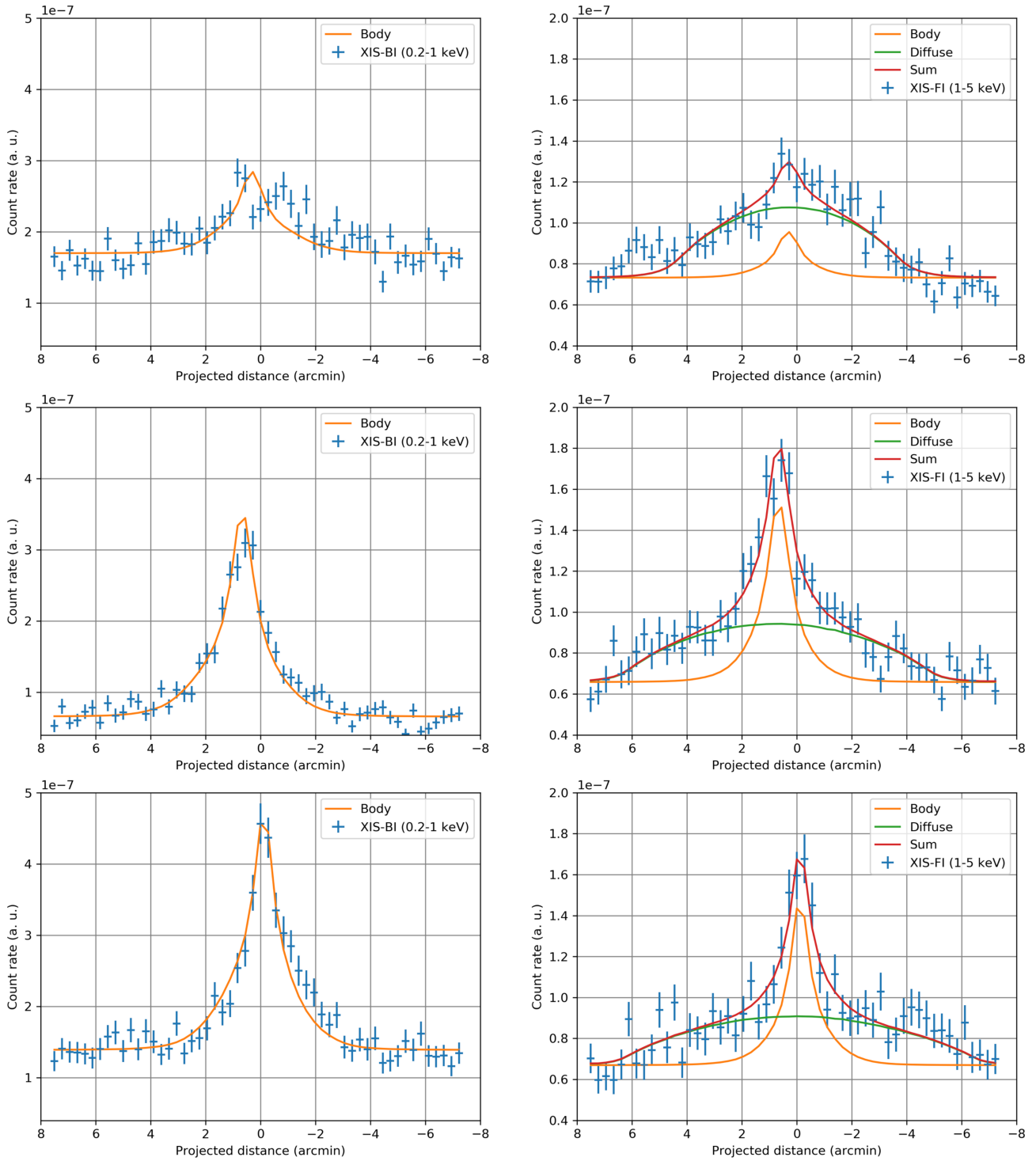
Fig. 4. Projection profiles in 0.2–1 keV (BI; left) and 1–5 keV (FI; right) along the horizontal axis, extracted from the rectangular regions in Figure 3, but with a binning of 16 × 16 pixels without smoothing. Crosses show the data. Errors are statistical 1σ ones. The orange curves both in the left and right panels show the profiles of Jupiter's body emissions, whereas the green curves in the right panels show the best-fit profile of uniform elliptical emissions (see the text). The red curves in the right panels indicate the sum of the orange and green curves.
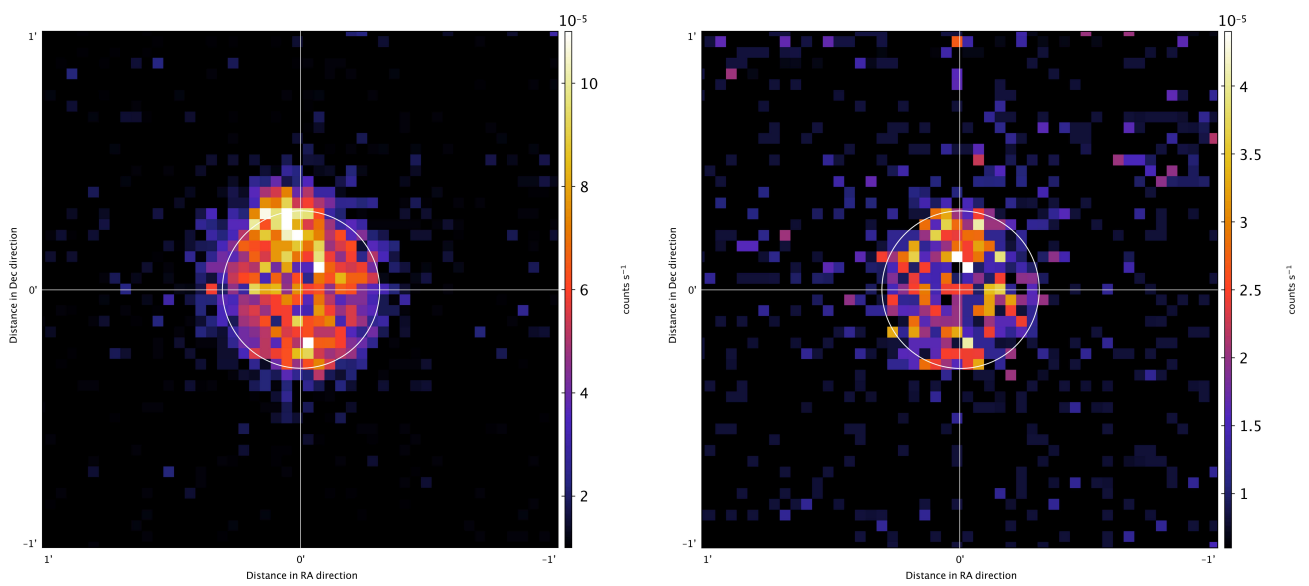
Fig. 5. XMM-Newton EPIC's combined images in 2014 after correcting for Jupiter's ephemeris and XMM-Newton's orbital motion in 0.2–1 (left) and 1–5 keV (right). Exposures are corrected so that the unit is counts s^{-1}. The images are not binned and smoothed. White circles have a radius of 18.3 arcsec. Both the width and the height of the image correspond to 2 arcmin.
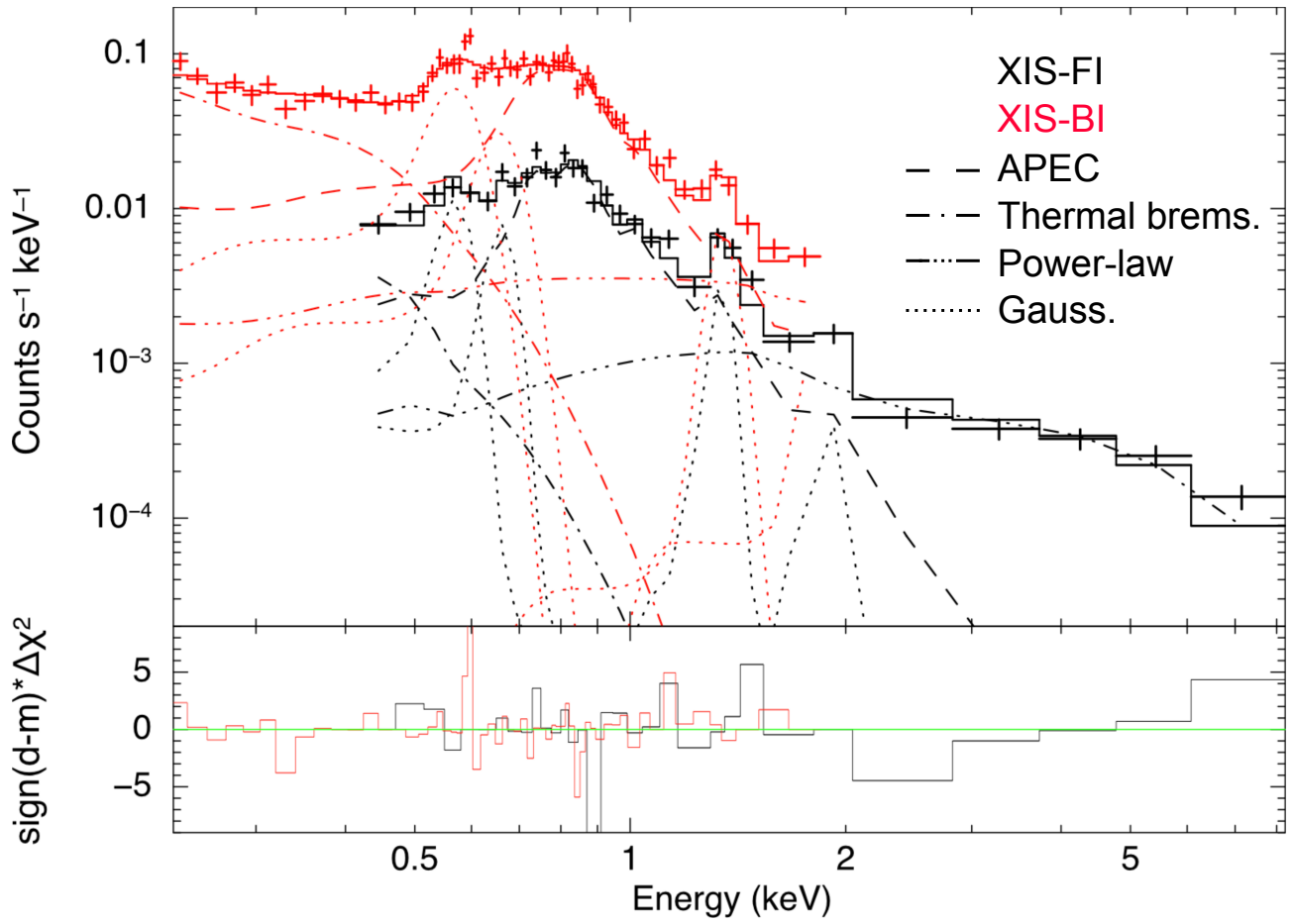
Fig. 6. Background-subtracted EPIC MOS (black) and pn (red) spectra of Jupiter's body emission region in 2014, compared with the best-fit models summarized in Table 2 (solid lines). APEC model, thermal bremsstrahlung, a power-law function, and four Gaussians are shown in dashed, dash-dotted, dash-three-dotted, and dotted lines, respectively.
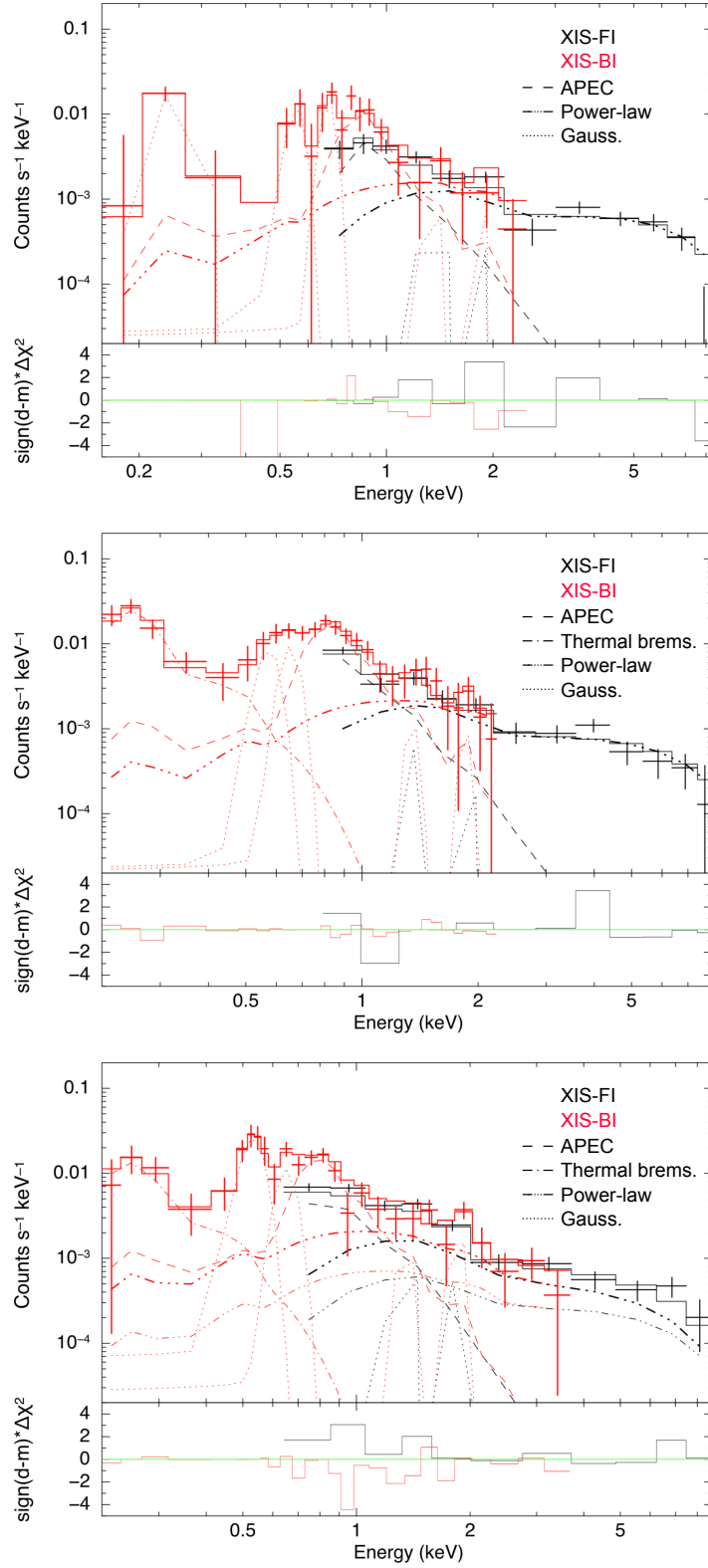
Fig. 7. Background-subtracted XIS FI (black) and BI (red) spectra of the extended emission region in 2006 (top), 2012 (middle), and 2014 (bottom), compared with the best-fit models summarized in Table 3 (solid lines). APEC model, thermal bremsstrahlung, one or two power-law functions, and four or five Gaussians are shown in dashed, dash-dotted, dash-three-dotted, and dotted lines, respectively.
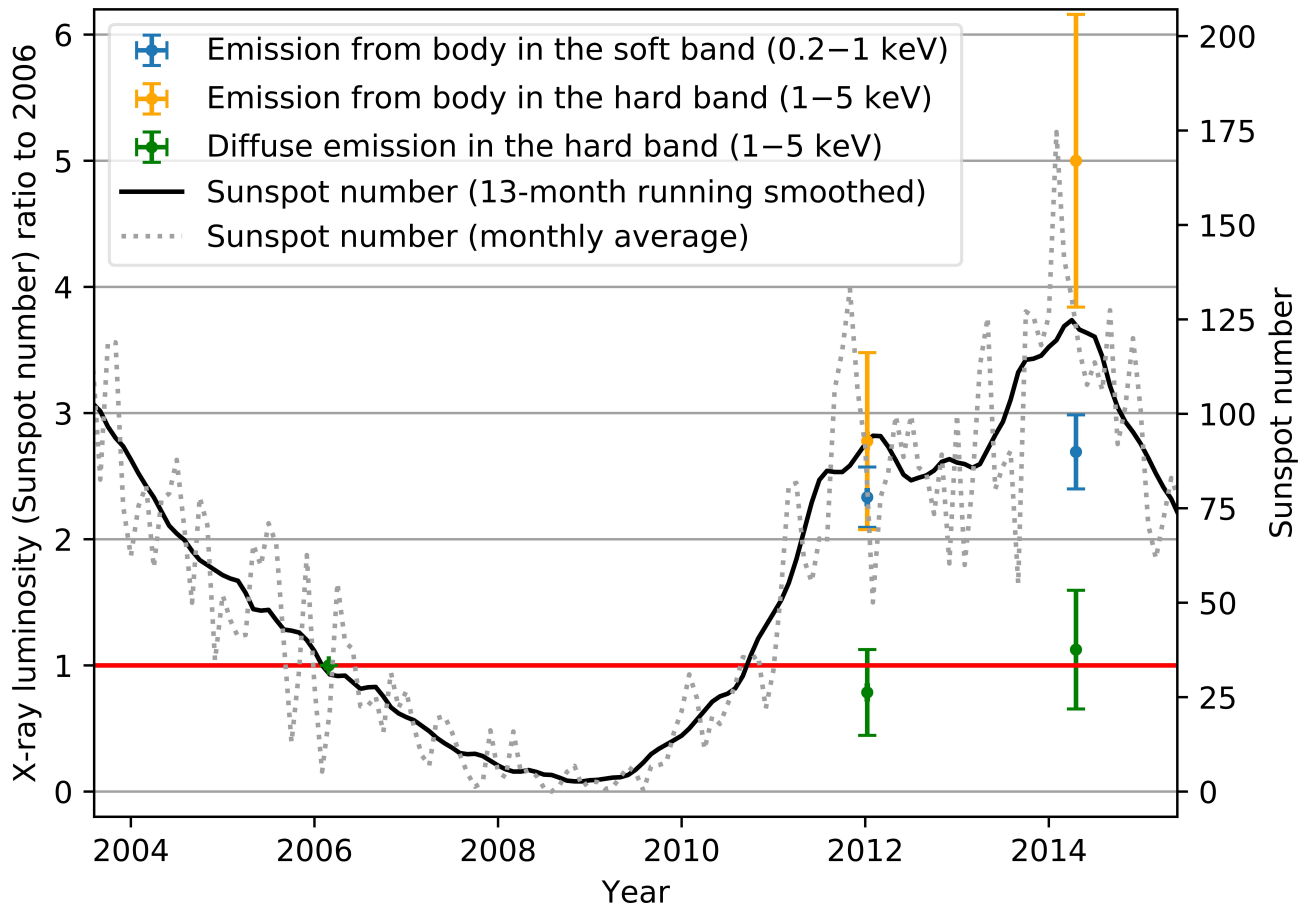
34

Fig. 8. Variations of the Suzaku observed X-ray luminosities of the emission from Jupiter's body in soft (0.2–1 keV) and hard (1–5 keV) bands and of the diffuse emission in the hard band, compared to that of the solar activity. Each colored mark indicates each luminosity as shown in the legend. A solid black line shows 13-month running smoothed sunspot number, while a dotted gray line shows monthly average ones. Vertical axes are luminosity ratios in the left side with each luminosity of the 2006 observation described as unity and sunspot number in the right side. Ratio of the sunspot number is also adjusted to its value on February 2006 in the left vertical axis. The sunspot data are obtained from a python package SunPy (version 1.1.0; The SunPy Community et al. 2015).
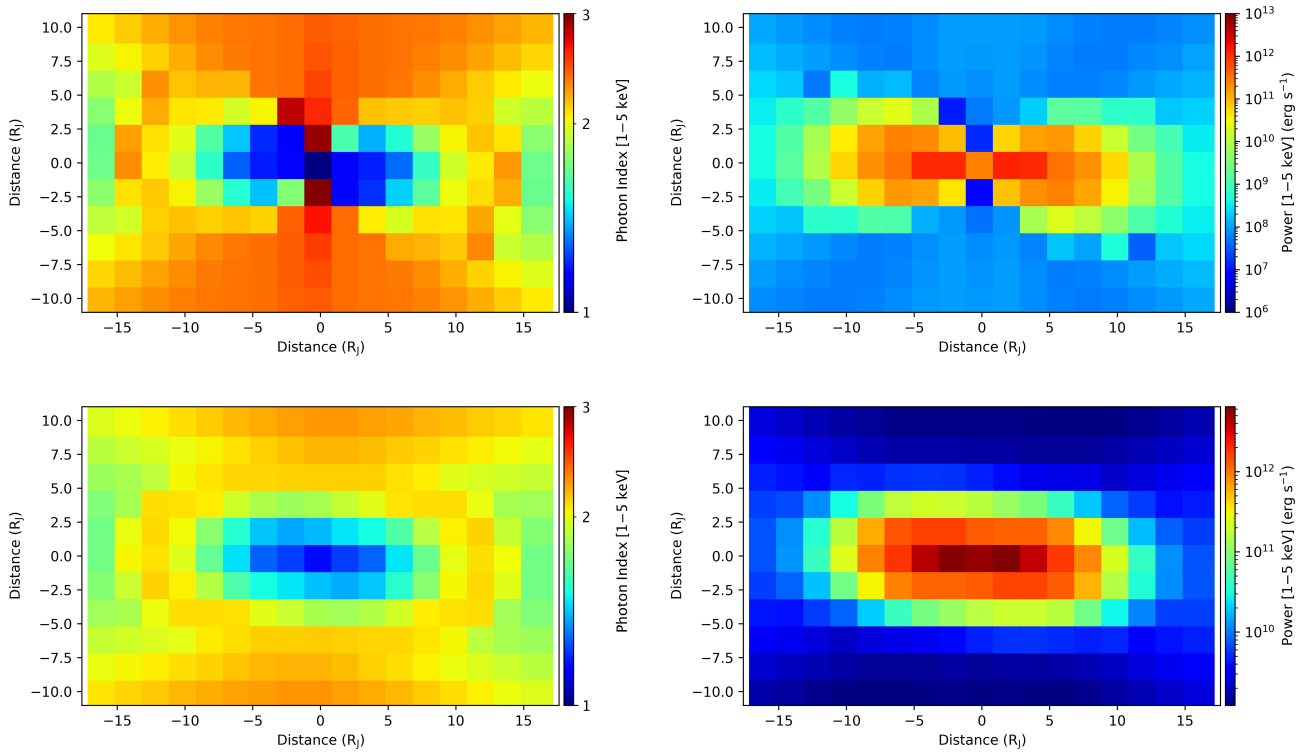
Fig. 9. The D&G-model calculated color maps in a certain meridian surface (top) and the three-dimensional ones (bottom) integrated in a direction of a line of sight of photon indexes of inverse-Comptonized 1–5 keV X-ray spectra (left), and powers of inverse-Comptonized 1–5 keV X-rays (right). The photon indexes are obtained by fitting to the photon spectrum with a power-law function at each location.
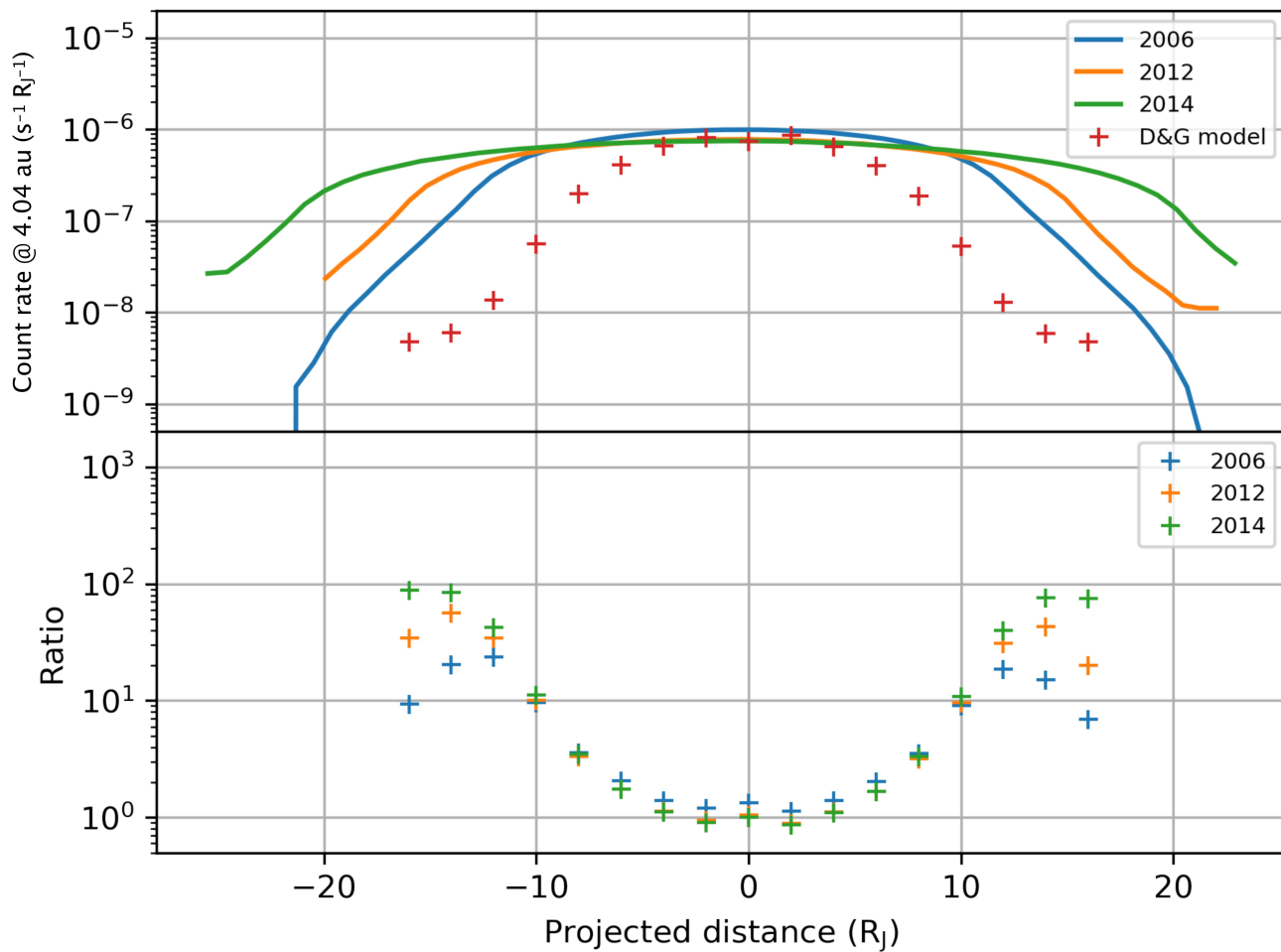
Fig. 10. (Top) Intensity profiles of the extended emission modeled by the elliptical shape for the three Suzaku observations, along with the D&G model prediction. The fittings with the elliptical shape are shown in Figure 4. Normalizations of these profiles are corrected so that every distance to Jupiter is 4.04 au. (Bottom) Intensity ratio to the D&G model. Errors are not shown in the plots.